

Dark Matter Model *or* Mass, but Not Both: Assessing Near-Future Direct Searches with Benchmark-free Forecasting

Thomas D. P. Edwards,* Bradley J. Kavanagh,† and Christoph Weniger‡
*Gravitation Astroparticle Physics Amsterdam (GRAPPA),
 Institute for Theoretical Physics Amsterdam and Delta Institute for Theoretical Physics,
 University of Amsterdam, Science Park 904, 1090 GL Amsterdam, The Netherlands*
 (Dated: November 14, 2018)

Forecasting the signal discrimination power of dark matter (DM) searches is commonly limited to a set of arbitrary benchmark points. We introduce new methods for benchmark-free forecasting that instead allow an exhaustive exploration and visualization of the phenomenological distinctiveness of DM models, based on standard hypothesis testing. Using this method, we reassess the signal discrimination power of future liquid Xenon and Argon direct DM searches. We quantify the parameter regions where various non-relativistic effective operators, millicharged DM, and magnetic dipole DM can be discriminated, and where upper limits on the DM mass can be found. We find that including an Argon target substantially improves the prospects for reconstructing the DM properties. We also show that only in a small region with DM masses in the range 20–100 GeV and DM-nucleon cross sections a factor of a few below current bounds can near-future Xenon and Argon detectors discriminate both the DM-nucleon interaction and the DM mass simultaneously. In all other regions only one or the other can be obtained.

Introduction.— Searching for the elusive Dark Matter (DM) particle has been the preoccupation of physicists for many years [1, 2]. Over the past decade, two-phase scintillator direct detection experiments [3, 4] have found much success with the LUX [5], XENON [6] and PANDA-X [7] collaborations providing the most stringent constraints on DM particles in the GeV – TeV mass range to date. Such experiments will continue to improve in sensitivity for many years to come. In the case of a detection, it should be possible to study the astrophysical and particle-physics properties of DM using a variety of detectors and detection methods (see [8–12] and many others), but the precise parameter regions in which these properties can actually be measured is hard to quantify.

Exploring the prospects for discriminating between different DM-nucleon interactions usually relies on comparing a number of benchmark models [13–19]. However, the pair-wise comparison of different benchmark points in the model parameter space (DM couplings or masses) is time-consuming, does not scale well with the number of benchmark points, and is in particular problematic in high-dimensional parameter spaces. In direct detection, such a high-dimensional parameter space appears in the framework of non-relativistic effective field theory (NREFT) [20–24], in which the space of DM-nucleon interactions may have more than 30 dimensions [25–27]. With current techniques, it is hence difficult to study model degeneracies and the degeneracy-breaking power of future instruments in a reliable and exhaustive way. For such tasks, dedicated techniques are required.

In this *Letter*, we introduce a new framework for studying the signal discrimination power of future detectors in

a fundamentally benchmark-free way. The key questions we aim to address are: How many *observationally distinct* signals does a given model predict for a set of future experiments? How many of these signals are compatible with specific subsets of the signal model? In which regions of parameter space is signal discrimination and parameter reconstruction possible?

We first summarize the basics of our approach. We then discuss the dark matter models and experiments we consider in the current work. Finally, we show our results and conclude with a short discussion about possible future directions and applications¹.

Information Geometry.— Consider a New-Physics model \mathcal{M} with some d -dim model parameter space, $\vec{\theta} \in \Omega_{\mathcal{M}} \in \mathbb{R}^d$, and a combination of future experiments X that are described by some likelihood function $\mathcal{L}_X(\mathcal{D}|\vec{\theta})$, where \mathcal{D} is data. We expect that two model parameter points $\vec{\theta}$, $\vec{\theta}'$ can be discriminated by experiments X if the parameter point $\vec{\theta}'$ is inconsistent with Asimov data [28] $\mathcal{D} = \bar{\mathcal{D}}(\vec{\theta})$. More concretely, distinctiveness requires that the log-likelihood ratio

$$\text{TS}(\vec{\theta}')_{\bar{\mathcal{D}}(\vec{\theta})} \equiv -2 \ln \frac{\mathcal{L}(\bar{\mathcal{D}}(\vec{\theta})|\vec{\theta}')}{\max_{\vec{\theta}''} \mathcal{L}(\bar{\mathcal{D}}(\vec{\theta})|\vec{\theta}'')} \simeq \|\vec{x}(\vec{\theta}) - \vec{x}(\vec{\theta}')\|^2, \quad (1)$$

exceeds a threshold value $r_{\alpha}(\mathcal{M})^2$. The threshold value depends on the chosen statistical significance, which we set here to $\alpha = 0.045$ (2σ), as well as the sampling distribution of $\text{TS}(\vec{\theta}')$. In the large-sample limit and under certain regularity conditions, the sampling distribution

* t.d.p.edwards@uva.nl

† b.j.kavanagh@uva.nl

‡ c.weniger@uva.nl

¹ Code associated with the paper available at https://github.com/tedwards2412/benchmark_free_forecasting/.

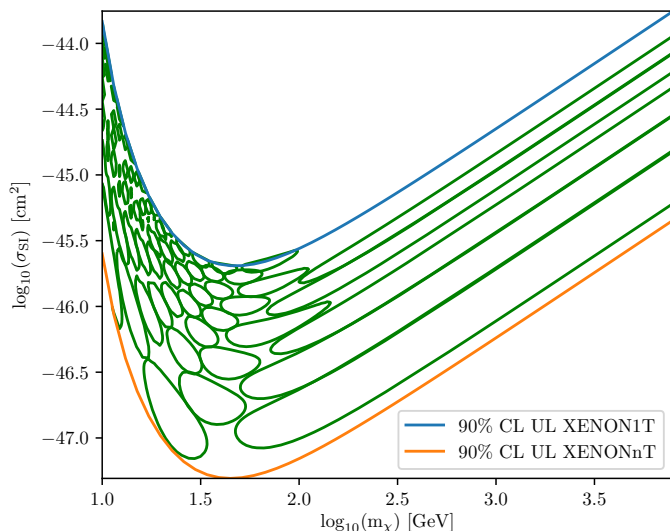


FIG. 1. Limit on the SI cross-section vs. DM mass, assuming operator \mathcal{O}_1 , for a XENONnT detector. Contours show 68% confidence contours in $d = 2$ dimensions. The radius of these contours in the Euclidean space is therefore $r_\alpha(\mathcal{M}) = 1.52$. The number of discriminable signals in the blue+blue/orange region of the middle panel of Fig. 2 can be approximated by counting the number of closed green contours.

follows a χ_k^2 distribution with $k = d$ degrees of freedom [28, 29].

The last part of Eq. (1) is an approximation based on the ‘euclideanized signal’ method [30], an embedding $\vec{\theta} \mapsto \vec{x}(\vec{\theta}) \in \mathbb{R}^n$ into some, usually higher-dimensional, space with unit Fisher information matrix (n usually equals the total number of data bins). This approximation maps statistical distinctiveness onto euclidean distances, and works to within 20% if the number of counts is order one, see [30] for a discussion and caveats. Confidence regions in the model parameter space correspond then to hyperspheres of radius $r_\alpha(\mathcal{M})$ in the euclideanized signal space.

Often one is interested in sub-models \mathcal{S} that are nested inside model \mathcal{M} , and which are obtained by restricting \mathcal{M} to a d' -dim subregion $\Omega_{\mathcal{S}} \subset \Omega_{\mathcal{M}}$. A parameter point $\vec{\theta}$ of \mathcal{M} leads to a signal that is distinct from any signal in submodel \mathcal{S} if

$$-2 \ln \frac{\max_{\vec{\theta}' \in \Omega_{\mathcal{S}}} \mathcal{L}(\bar{\mathcal{D}}(\vec{\theta})|\vec{\theta}')}{\max_{\vec{\theta}'} \mathcal{L}(\bar{\mathcal{D}}(\vec{\theta})|\vec{\theta}')} \simeq \min_{\vec{\theta}' \in \Omega_{\mathcal{S}}} \|\vec{x}(\vec{\theta}) - \vec{x}(\vec{\theta}')\|^2, \quad (2)$$

exceeds a certain threshold value $r_\alpha(\mathcal{S}, \mathcal{M})^2$. Here ‘distinct’ means that the composite null hypothesis \mathcal{S} can be rejected for data $\bar{\mathcal{D}}(\vec{\theta})$. The sampling distribution of Eq. (2) follows in general a $\chi_{k=d-d'}^2$ distribution. In the euclideanized signal space \vec{x} , parts of model \mathcal{M} cannot be discriminated from model \mathcal{S} that lie within a ‘shell’ of thickness $r_\alpha(\mathcal{S}, \mathcal{M})$ around the signal manifold of \mathcal{S} .

Finally, nuisance parameters can be accounted for by replacing the likelihood function in Eq. (1) with a pro-

file likelihood, $\mathcal{L}(\mathcal{D}|\vec{\theta}) = \max_{\vec{\eta}} \mathcal{L}(\mathcal{D}|\vec{\theta}, \vec{\eta}) \mathcal{L}_\eta(\vec{\eta})$, where the last factor can incorporate additional constraints on the nuisance parameters from data external to X .

Distinct signals.— To quantify the signal discrimination power of a set of future experiments X in the context of model \mathcal{M} we may define the figure of merit

$$\nu_{\mathcal{M}, X}^\alpha(\Omega_{\mathcal{M}}) \simeq \begin{array}{l} \text{Total number of signals from model } \mathcal{M} \\ \text{discriminable by experiments } X. \end{array}$$

More specifically, $\nu_{\mathcal{M}, X}^\alpha$ equals the maximum number of points that can populate the parameter space of \mathcal{M} while remaining mutually distinct according to Eq. (1). Any such set of points provides a complete sample of the phenomenological features of model \mathcal{M} . Loosely speaking, the points correspond to a set of non-overlapping confidence contours as shown in Fig. 1. Furthermore, when considering a sub-model \mathcal{S} nested in \mathcal{M} , we can define

$$\begin{array}{l} \text{Number of signals from model } \mathcal{M} \text{ dis-} \\ \text{criminable by experiments } X, \text{ and con-} \\ \text{sistent with model } \mathcal{S}. \end{array} \quad (3)$$

With these definitions, the phenomenological distinctiveness of various regions in the parameter space of model \mathcal{M} can be visualized using standard Venn diagrams [31]. The technical definition for the measure $\nu_{\mathcal{M}, X}^\alpha(\cdot)$, which is used in the subsequent examples, is given in Appendix A of the Supplemental Material.

DM-nucleon interactions.— While direct detection is typically analysed in terms of the standard spin-dependent (SD) and spin-independent (SI) interactions [32], the range of possible signals is much broader. The framework of non-relativistic effective field theory (NREFT) [20–24] aims to classify possible elastic DM-nucleon interactions and thus possible signals in DM-nucleus scattering experiments. NREFT is realised as a power series in the DM-nucleus relative velocity \vec{v} and the nuclear recoil momentum \vec{q} , valid for non-relativistic, short-range interactions. The resulting operators (labelled $\mathcal{O}_1, \mathcal{O}_3, \mathcal{O}_4, \dots$) give rise to a range of novel energy spectra [14, 16, 19, 33], directional signals [34, 35] and annual modulation signatures [36, 37]. We focus here on the three operators $\mathcal{O}_1, \mathcal{O}_4$ and \mathcal{O}_{11} because they allow us to explore a diverse range of signals with only a small number of operators². Operator $\mathcal{O}_1 = 1_\chi 1_N$ couples to nucleon number while the operator $\mathcal{O}_4 = \vec{S}_\chi \cdot \vec{S}_N$ couples to nuclear spin, allowing us to explore the complementarity between nuclei of different size and spin [40]. Operator $\mathcal{O}_{11} = i\vec{q} \cdot \vec{S}_\chi / m_N$ may arise as the leading-order interaction in certain scalar-mediated models [24]. Similar to \mathcal{O}_1 , it also couples to nucleon number and receives a coherent enhancement to the rate, but has a characteristic peaked recoil spectrum owing to an extra $d\sigma/dE_R \propto E_R$

² We neglect the effects of operator mixing [38, 39] which require us to specify the structure of the dark sector.

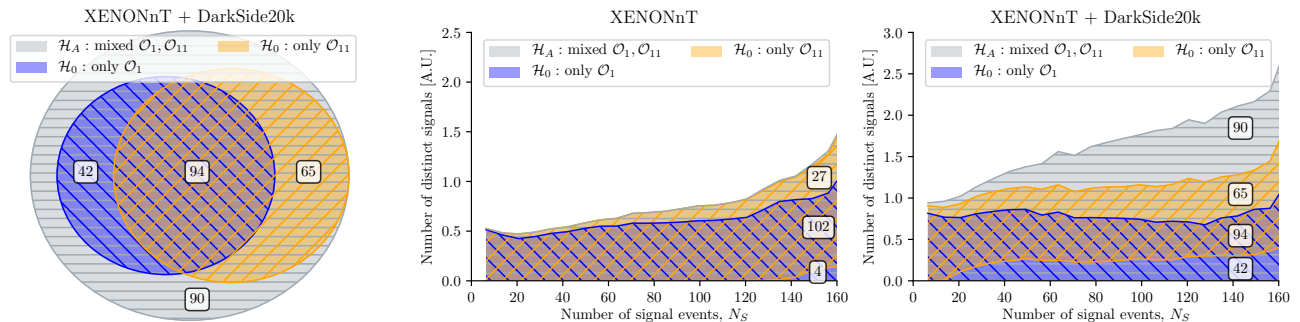


FIG. 2. Signal-discrimination power of combinations of direct detection experiments, summarized in *infometric Venn diagrams*. *Central/Right panel*: The full area corresponds to the *number of distinct detectable signals* within the alternative hypothesis \mathcal{H}_A , unfolded as function of number of XENONnT signal events. The subsets indicate the fraction of signals consistent with various null hypotheses \mathcal{H}_0 . Overlapping subsets correspond to signals consistent with multiple null hypotheses simultaneously. The numbers correspond to $\nu_{\mathcal{M},X}(\Omega_{\mathcal{M}})$ in each region. In the right panel, the overlapping (blue+orange) region corresponds to the model parameters between the purple-dot-dashed and orange contours in Fig. 3. The non-overlapping (blue-only) \mathcal{O}_1 region corresponds to parameters between the purple-dashed and blue contours in Fig. 3. *Left panel*: Standard Venn diagram summed over number of signal events.

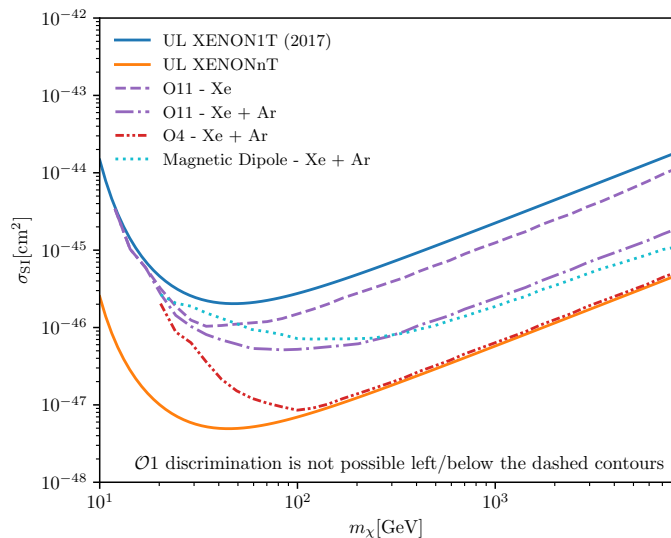


FIG. 3. Discriminability of DM interactions. To the left/below each broken line, it is not possible to discriminate an \mathcal{O}_1 -signal (with the indicated cross-section and DM mass) from the corresponding best-fit \mathcal{O}_4 , \mathcal{O}_{11} or magnetic dipole signal. Above/right of each broken line, such a discrimination is possible with at least 2σ significance. Solid lines display 90% CL limits for XENON1T-2017 and XENONnT. All lines include DM halo uncertainties.

scaling of the cross section [16]. This allows us to explore how well different recoil spectra can be discriminated in future experiments.

Unfortunately, NREFT cannot encompass all possible signals. In particular, in its original formulation [21] it cannot describe interactions through light mediators. In this case, the typical momentum transfer is larger than the mediator mass and an expansion in q is

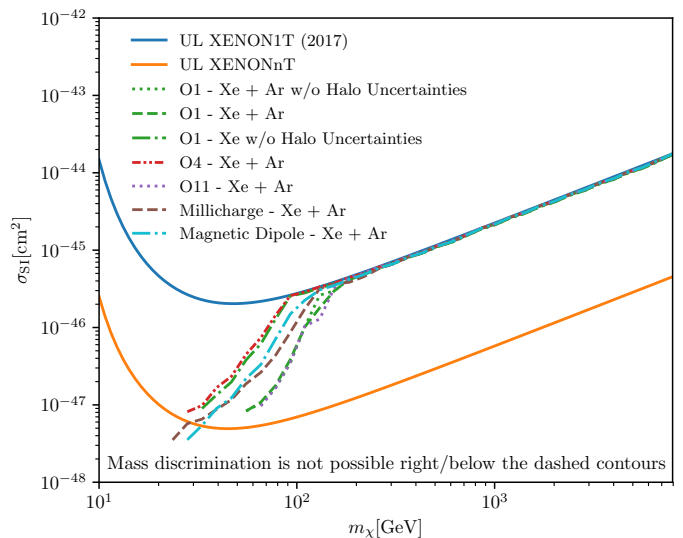


FIG. 4. Discriminability of the DM mass. To the right of each broken line, the DM mass is unbounded from above (at 2σ). Lines for other operators are mapped onto σ_{SI} by converting to an effective cross section and rescaled to match \mathcal{O}_1 at high masses. For \mathcal{O}_1 , we also show constraints for the Xenon-only case and when halo uncertainties are neglected. Solid lines display 90% CL limits for XENON1T-2017 and XENONnT.

no longer appropriate³. The scenario in which this mediator is the Standard Model photon has been studied extensively [41, 43, 44]. Here, we consider millicharged DM [45] which has long-ranged, coherently-enhanced interactions with nuclei, with a differential cross section

³ Note, however, that because the DM is still non-relativistic, the effects of light mediators can be incorporated into the NREFT by including the appropriate propagator [41, 42].

scaling as E_R^{-2} [41, 46, 47]. Alternatively, DM may have non-zero electric and magnetic moments [48, 49], particularly if it takes the form of a composite state, such as a Dark Baryon [50, 51]. In the context of model discrimination, most interesting for us will be the magnetic dipole, $(\mu_\chi/2) \bar{\chi} \sigma^{\mu\nu} \chi F_{\mu\nu}$, which leads to both long-range and short-range contributions to the rate, arising from charge-dipole and dipole-dipole interactions respectively [44, 52, 53].

The five DM-nucleon interaction models we have outlined above encompass a range of phenomenologically-driven as well as more theoretically-motivated models, leading to a wide range of direct detection signals. We calculate the signal spectra in each case using the publicly-available code `WIMpy` [54], implementing expressions from [23] and [41]⁴. The required nuclear response functions are taken from the `mathematica` package provided in [23], supplemented by those calculated in [55]. We assume iso-spin conserving ($c_p = c_n$) NREFT interactions and that the particle producing a signature makes up 100% of the local DM density (which we fix to $\rho_\chi = 0.3 \text{ GeV cm}^{-3}$ [56, 57]). We incorporate standard Gaussian halo uncertainties from [57]; details can be found in Appendix B of the Supplemental Material.

Direct dark matter searches.— We implement two toy detectors, designed to resemble the expected advancement in direct DM searches over the upcoming 5-10 years.

We implement a Xenon detector in light of the stringent constraints on $\mathcal{O}(10) \text{ GeV}$ DM set by XENON1T [6], with numerous Xenon-based experiments on the horizon [58–61]. We model this detector on the future *XENONnT* [60] experiment. In addition we implement a detector containing a target material with no nuclear spin, namely Argon, modeling this detector on *DarkSide20k* [62]. In this way we maximize discriminability of spin-dependent operators⁵. Our detector implementations and background assumptions are briefly described in Appendix B of the Supplemental Material.

Results.— In Fig. 1, we show the expected 68% CL reconstruction regions for a set of mutually distinct parameter points, for our *XENONnT*-like detector. The confidence regions are constructed by querying spheres with radius $r_\alpha(\mathcal{M}) = 1.52$ in the euclideanized signal space. The number of these regions corresponds approximately to the figure of merit in Eq. (3).

In the central panel of Fig. 2, we illustrate the power of *XENONnT* to discriminate between operators in the 3-dimensional model space \mathcal{M} of mass, \mathcal{O}_1 , and \mathcal{O}_{11} . With increasing numbers of events, the number of discriminable signals increases, though the majority of signals are compatible with both \mathcal{O}_1 and \mathcal{O}_{11} . In the right

panel of Fig. 2, we include also information from *DarkSide20k*. The addition of an Argon detector not only increases the number of discriminable signals (from 133 to 291) but also enlarges the region of parameter space where \mathcal{O}_1 and \mathcal{O}_{11} can be discriminated from each other. The left panel of Fig. 2 corresponds to the same scenario as the right panel, instead summed over the number of *XENONnT* signal events. 160 signal events approximately corresponds the expected number of events in XENON-nT if the true model were at the current sensitivity. We note that the Venn diagrams we have introduced here significantly increase in complexity when comparing a large number of models at once. However, we emphasize that the number of discriminable regions, Eq. (3), is completely general and remains a useful measure for assessing model discriminability.

Figure 3 shows the regions of the parameter space of spin-independent (\mathcal{O}_1) DM in which discrimination from \mathcal{O}_4 , \mathcal{O}_{11} and magnetic dipole DM would be possible. For \mathcal{O}_4 (spin-dependent), 2σ discrimination is possible at high DM mass even down to small cross sections, when both Xenon and Argon experiments are used. The spin-zero Argon nucleus has no spin-dependent coupling, so we can discriminate well as long as the Argon detector has sensitivity ($m_\chi > \mathcal{O}(20 \text{ GeV})$, below which most recoils are below the 32 keV threshold).

For \mathcal{O}_{11} , discrimination is possible at high mass because of the different spectral shapes of \mathcal{O}_1 and \mathcal{O}_{11} , though cross sections around $\sim 10^{-46} \text{ cm}^2$ are required to obtain enough events to map out the spectra precisely. At low mass, the peak in the \mathcal{O}_{11} spectrum falls below the threshold of the experiments; for both \mathcal{O}_1 and \mathcal{O}_{11} the exponentially falling tail of the DM velocity distribution dominates the spectral shape [63], making discrimination impossible.

For Magnetic Dipole interactions, discrimination is also possible at high mass, given enough signal events. We note a ‘kink’ in the boundary for Magnetic Dipole interactions around $m_\chi \sim 20 \text{ GeV}$. For large DM masses, the short-range spin-dependent dipole-dipole contribution begins to dominate [44]. In this case, discrimination prospects are good with the inclusion of the spin-zero Argon detector.

For the mock detectors we consider, SI interactions cannot be distinguished from Millicharged DM, which is not shown in Fig. 3. The recoil spectrum for Millicharged DM is similar to \mathcal{O}_1 , but has an extra E_R^{-2} suppression. This more rapidly falling recoil spectrum can be mimicked by an SI interaction with smaller DM mass. As demonstrated in Refs. [16, 42], low-threshold semi-conductor experiments are required to distinguish between the two interactions.

Finally, Fig. 4 shows, for various operators, the regions of parameter space where a closed contour for the DM mass would be possible at the 2σ level. At large DM masses, the kinematics of the interaction mean that the recoil spectrum becomes independent of the DM mass, meaning that to the right of the curves in Fig. 4, it is

⁴ Note that the operator normalisations in [41] and [23] differ.

⁵ Liquid noble detectors typically do not have sensitivity to DM particles lighter than a few GeV, so we restrict our attention to $m_\chi > 10 \text{ GeV}$ in the current work.

not possible to obtain an upper limit on m_χ [64, 65]. For \mathcal{O}_1 we show the regions for Xenon-only, as well as for Xenon and Argon combined without halo uncertainties to demonstrate the improvement in mass reconstruction when including a second detector. When the two detectors are combined halo uncertainties make little difference to the mass discrimination, as changes in the velocity distribution affect the spectra in the two detectors differently [8]. Operator \mathcal{O}_4 contains the largest region in which the mass cannot be constrained due to the lack of signal in Argon.

Even in the most optimistic case of cross sections just below the current bounds, it is not possible to pin down the DM mass for $m_\chi \gtrsim 100$ GeV. Previous works have demonstrated, typically using a small number of benchmarks [16, 65, 66], that DM mass reconstruction worsens for large masses; here, we have mapped out precisely where this mass reconstruction fails as a function of mass and cross section.

Discussion.— The methods introduced in this paper allow us to efficiently characterize and visualize the phenomenological distinctiveness of direct DM signal models in infometric Venn diagrams, as shown in Fig. 2. Furthermore, these methods allow for an efficient exploration of the phenomenology of complex models, and hence allow us to make ‘benchmark-free’ statements like those shown in Figs. 3 and 4. In Fig. 3 we see that ruling out non-standard interactions is harder for light DM, while in Fig. 4 we see that we cannot pin down the DM mass for masses larger than ~ 100 GeV. This leaves only a small region of parameter space – for $m_\chi \in [20, 100]$ GeV and cross sections a factor of a few below current bounds – in which the DM mass and interaction can both be constrained at the 2σ level with near-future Xenon and Argon detectors. Such general statements would not have been possible without an efficient exploration of the Dark Matter parameter space, made feasible with the tools presented here. Third generation experiments such as DARWIN [59] will have a far greater sensitivity. More events would dramatically improve our ability to con-

strain different models, particularly for models at the current XENON1T bound.

This work paves the way for a more complete exploration of the direct detection parameter space and a deeper understanding of the complementarity between detectors. Future work should explore the possibility to discriminate between a wider range of interactions, beyond the subset of five we include here. In addition, the techniques we present may be used to optimize detector properties (target material, thresholds, etc.) in order to understand how operator discrimination can be improved at low DM mass.

Our ‘benchmark-free’ method rests on the ‘euclideanised signal’ introduced in [30], and works for any Poisson (and hence Gaussian) likelihood function, as long as background uncertainties are sufficiently Gaussian. Euclideanised signals therefore provide a useful forecasting tool for a wide range of New-Physics signals, including those in cosmology, indirect DM detection, and collider searches. As we have shown, using direct detection alone may not allow us to completely constrain the DM properties. Combining complementary information from other search strategies, coupled with new techniques for efficient forecasting, will provide essential guidance in the future of Dark Matter detection.

ACKNOWLEDGMENTS

The authors thank Riccardo Catena for sharing fortran routines to calculate nuclear structure functions. In addition we thank the GAMBIT collaboration for extensive discussions on future direct detection instruments. We also thank Felix Kahlhoefer, Christopher McCabe, and Mauro Valli for very helpful comments on this manuscript. Finally, we thank the python scientific computing packages numpy [67] and scikit-learn [68]. This research is funded by NWO through the VIDI research program “Probing the Genesis of Dark Matter” (680-47-532; TE, CW, BK).

-
- [1] G. Jungman, M. Kamionkowski, and K. Griest, Phys. Rept. **267**, 195 (1996), arXiv:hep-ph/9506380 [hep-ph].
 - [2] G. Bertone, D. Hooper, and J. Silk, Phys. Rept. **405**, 279 (2005), arXiv:hep-ph/0404175 [hep-ph].
 - [3] M. W. Goodman and E. Witten, Phys. Rev. **D31**, 3059 (1985), [,325(1984)].
 - [4] A. K. Drukier, K. Freese, and D. N. Spergel, Phys. Rev. **D33**, 3495 (1986).
 - [5] D. S. Akerib *et al.* (LUX), Phys. Rev. Lett. **118**, 021303 (2017), arXiv:1608.07648 [astro-ph.CO].
 - [6] E. Aprile *et al.* (XENON), Phys. Rev. Lett. **119**, 181301 (2017), arXiv:1705.06655 [astro-ph.CO].
 - [7] X. Cui *et al.* (PandaX-II), Phys. Rev. Lett. **119**, 181302 (2017), arXiv:1708.06917 [astro-ph.CO].
 - [8] A. H. G. Peter, V. Gluscevic, A. M. Green, B. J. Kavanagh, and S. K. Lee, Phys. Dark Univ. **5-6**, 45 (2014), arXiv:1310.7039 [astro-ph.CO].
 - [9] B. J. Kavanagh, M. Fornasa, and A. M. Green, Phys. Rev. **D91**, 103533 (2015), arXiv:1410.8051 [astro-ph.CO].
 - [10] M. Cahill-Rowley, R. Cotta, A. Drlica-Wagner, S. Funk, J. Hewett, A. Ismail, T. Rizzo, and M. Wood, Phys. Rev. **D91**, 055011 (2015), arXiv:1405.6716 [hep-ph].
 - [11] A. Alves, A. Berlin, S. Profumo, and F. S. Queiroz, Phys. Rev. **D92**, 083004 (2015), arXiv:1501.03490 [hep-ph].
 - [12] G. Bertone, N. Bozorgnia, J. S. Kim, S. Liem, C. McCabe, S. Otten, and R. Ruiz de Austri, JCAP **1803**, 026 (2018), arXiv:1712.04793 [hep-ph].
 - [13] R. Catena, JCAP **1407**, 055 (2014), arXiv:1406.0524 [hep-ph].

- [14] M. I. Gresham and K. M. Zurek, Phys. Rev. **D89**, 123521 (2014), arXiv:1401.3739 [hep-ph].
- [15] V. Gluscevic and A. H. G. Peter, JCAP **1409**, 040 (2014), arXiv:1406.7008 [astro-ph.CO].
- [16] V. Gluscevic, M. I. Gresham, S. D. McDermott, A. H. G. Peter, and K. M. Zurek, JCAP **1512**, 057 (2015), arXiv:1506.04454 [hep-ph].
- [17] F. Kahlhoefer and S. Wild, JCAP **1610**, 032 (2016), arXiv:1607.04418 [hep-ph].
- [18] R. Catena, J. Conrad, C. Dring, A. D. Ferella, and M. B. Krauss, (2017), arXiv:1706.09471 [hep-ph].
- [19] S. Baum, R. Catena, J. Conrad, K. Freese, and M. B. Krauss, (2017), arXiv:1709.06051 [hep-ph].
- [20] J. Fan, M. Reece, and L.-T. Wang, JCAP **1011**, 042 (2010), arXiv:1008.1591 [hep-ph].
- [21] A. L. Fitzpatrick, W. Haxton, E. Katz, N. Lubbers, and Y. Xu, JCAP **1302**, 004 (2013), arXiv:1203.3542 [hep-ph].
- [22] A. L. Fitzpatrick, W. Haxton, E. Katz, N. Lubbers, and Y. Xu, (2012), arXiv:1211.2818 [hep-ph].
- [23] N. Anand, A. L. Fitzpatrick, and W. C. Haxton, Phys. Rev. **C89**, 065501 (2014), arXiv:1308.6288 [hep-ph].
- [24] J. B. Dent, L. M. Krauss, J. L. Newstead, and S. Sabharwal, Phys. Rev. **D92**, 063515 (2015), arXiv:1505.03117 [hep-ph].
- [25] R. Catena, JCAP **1409**, 049 (2014), arXiv:1407.0127 [hep-ph].
- [26] R. Catena and P. Gondolo, JCAP **1409**, 045 (2014), arXiv:1405.2637 [hep-ph].
- [27] R. Catena and P. Gondolo, JCAP **1508**, 022 (2015), arXiv:1504.06554 [hep-ph].
- [28] G. Cowan, K. Cranmer, E. Gross, and O. Vitells, Eur. Phys. J. **C71**, 1554 (2011), [Erratum: Eur. Phys. J. **C73**, 2501(2013)], arXiv:1007.1727 [physics.data-an].
- [29] S. S. Wilks, Annals Math. Statist. **9**, 60 (1938).
- [30] T. D. P. Edwards and C. Weniger, (2017), arXiv:1712.05401 [hep-ph].
- [31] J. Venn, The London, Edinburgh, and Dublin Philosophical Magazine and Journal of Science **10**, 1 (1880).
- [32] D. G. Cerdeno and A. M. Green, “Direct detection of WIMPs,” in *Particle Dark Matter: Observations, Models and Searches*, edited by G. Bertone (2010) pp. 347–369, arXiv:1002.1912 [astro-ph.CO].
- [33] S. Chang, A. Pierce, and N. Weiner, JCAP **1001**, 006 (2010), arXiv:0908.3192 [hep-ph].
- [34] R. Catena, JCAP **1507**, 026 (2015), arXiv:1505.06441 [hep-ph].
- [35] B. J. Kavanagh, Phys. Rev. **D92**, 023513 (2015), arXiv:1505.07406 [hep-ph].
- [36] E. Del Nobile, G. B. Gelmini, and S. J. Witte, Phys. Rev. **D91**, 121302 (2015), arXiv:1504.06772 [hep-ph].
- [37] E. Del Nobile, G. B. Gelmini, and S. J. Witte, JCAP **1602**, 009 (2016), arXiv:1512.03961 [hep-ph].
- [38] F. D’Eramo, B. J. Kavanagh, and P. Panci, JHEP **08**, 111 (2016), arXiv:1605.04917 [hep-ph].
- [39] F. Bishara, J. Brod, B. Grinstein, and J. Zupan, (2017), arXiv:1708.02678 [hep-ph].
- [40] D. G. Cerdeo *et al.*, JCAP **1307**, 028 (2013), [Erratum: JCAP1309,E01(2013)], arXiv:1304.1758 [hep-ph].
- [41] M. Cirelli, E. Del Nobile, and P. Panci, JCAP **1310**, 019 (2013), arXiv:1307.5955 [hep-ph].
- [42] F. Kahlhoefer, S. Kulkarni, and S. Wild, JCAP **1711**, 016 (2017), arXiv:1707.08571 [hep-ph].
- [43] C. M. Ho and R. J. Scherrer, Phys. Lett. **B722**, 341 (2013), arXiv:1211.0503 [hep-ph].
- [44] E. Del Nobile, G. B. Gelmini, P. Gondolo, and J.-H. Huh, JCAP **1406**, 002 (2014), arXiv:1401.4508 [hep-ph].
- [45] S. D. McDermott, H.-B. Yu, and K. M. Zurek, Phys. Rev. **D83**, 063509 (2011), arXiv:1011.2907 [hep-ph].
- [46] N. Fornengo, P. Panci, and M. Regis, Phys. Rev. **D84**, 115002 (2011), arXiv:1108.4661 [hep-ph].
- [47] P. Panci, Adv. High Energy Phys. **2014**, 681312 (2014), arXiv:1402.1507 [hep-ph].
- [48] K. Sigurdson, M. Doran, A. Kurylov, R. R. Caldwell, and M. Kamionkowski, Phys. Rev. **D70**, 083501 (2004), [Erratum: Phys. Rev. **D73**, 089903(2006)], arXiv:astro-ph/0406355 [astro-ph].
- [49] T. Banks, J.-F. Fortin, and S. Thomas, (2010), arXiv:1007.5515 [hep-ph].
- [50] J. Bagnasco, M. Dine, and S. D. Thomas, Phys. Lett. **B320**, 99 (1994), arXiv:hep-ph/9310290 [hep-ph].
- [51] T. Banks, J. D. Mason, and D. O’Neil, Phys. Rev. **D72**, 043530 (2005), arXiv:hep-ph/0506015 [hep-ph].
- [52] V. Barger, W.-Y. Keung, and D. Marfatia, Phys. Lett. **B696**, 74 (2011), arXiv:1007.4345 [hep-ph].
- [53] E. Del Nobile, C. Kouvaris, P. Panci, F. Sannino, and J. Virkajarvi, JCAP **1208**, 010 (2012), arXiv:1203.6652 [hep-ph].
- [54] B. J. Kavanagh and T. D. P. Edwards, “WIMpy_NREFT v1.0 [Computer Software], doi:10.5281/zenodo.1230503. Available at https://github.com/bradkav/WIMpy_NREFT,” (2018).
- [55] R. Catena and B. Schwabe, JCAP **1504**, 042 (2015), arXiv:1501.03729 [hep-ph].
- [56] J. I. Read, J. Phys. **G41**, 063101 (2014), arXiv:1404.1938 [astro-ph.GA].
- [57] A. M. Green, J. Phys. **G44**, 084001 (2017), arXiv:1703.10102 [astro-ph.CO].
- [58] D. S. Akerib *et al.* (LZ), (2015), arXiv:1509.02910 [physics.ins-det].
- [59] J. Aalbers *et al.* (DARWIN), JCAP **1611**, 017 (2016), arXiv:1606.07001 [astro-ph.IM].
- [60] G. Plante (XENON), <https://conferences.pa.ucla.edu/dm16/talks/plante.pdf> (2016).
- [61] D. S. Akerib *et al.* (LUX-ZEPLIN), (2018), arXiv:1802.06039 [astro-ph.IM].
- [62] C. E. Aalseth *et al.*, Eur. Phys. J. Plus **133**, 131 (2018), arXiv:1707.08145 [physics.ins-det].
- [63] J. D. Lewin and P. F. Smith, Astropart. Phys. **6**, 87 (1996).
- [64] A. M. Green, JCAP **0708**, 022 (2007), arXiv:hep-ph/0703217 [hep-ph].
- [65] A. M. Green, JCAP **0807**, 005 (2008), arXiv:0805.1704 [hep-ph].
- [66] J. L. Newstead, T. D. Jacques, L. M. Krauss, J. B. Dent, and F. Ferrer, Phys. Rev. **D88**, 076011 (2013), arXiv:1306.3244 [astro-ph.CO].
- [67] T. E. Oliphant, *Guide to NumPy*, 2nd ed. (CreateSpace Independent Publishing Platform, USA, 2015).
- [68] F. Pedregosa, G. Varoquaux, A. Gramfort, V. Michel, B. Thirion, O. Grisel, M. Blondel, P. Prettenhofer, R. Weiss, V. Dubourg, J. Vanderplas, A. Passos, D. Cournapeau, M. Brucher, M. Perrot, and E. Duchesnay, Journal of Machine Learning Research **12**, 2825 (2011).
- [69] E. W. Weisstein, “Hypersphere packing,” .
- [70] J. Bovy *et al.*, Astrophys. J. **759**, 131 (2012), arXiv:1209.0759 [astro-ph.GA].
- [71] S. E. Koposov, H.-W. Rix, and D. W. Hogg, Astrophys.

- J. **712**, 260 (2010), arXiv:0907.1085 [astro-ph.GA].
- [72] T. Piffi *et al.*, *Astron. Astrophys.* **562**, A91 (2014), arXiv:1309.4293 [astro-ph.GA].
- [73] A. H. G. Peter, *Phys. Rev.* **D81**, 087301 (2010), arXiv:0910.4765 [astro-ph.CO].
- [74] L. E. Strigari and R. Trotta, *JCAP* **0911**, 019 (2009), arXiv:0906.5361 [astro-ph.HE].
- [75] M. Pato, L. E. Strigari, R. Trotta, and G. Bertone, *JCAP* **1302**, 041 (2013), arXiv:1211.7063 [astro-ph.CO].
- [76] M. Schumann, L. Baudis, L. Btikofer, A. Kish, and M. Selvi, *JCAP* **1510**, 016 (2015), arXiv:1506.08309 [physics.ins-det].
- [77] J. L. Feng, J. Kumar, D. Marfatia, and D. Sanford, *Phys. Lett.* **B703**, 124 (2011), arXiv:1102.4331 [hep-ph].
- [78] P. Agnes *et al.* (DarkSide), *Phys. Lett.* **B743**, 456 (2015), arXiv:1410.0653 [astro-ph.CO].

SUPPLEMENTAL MATERIAL

Appendix A: Technical details

First, we generate a large number of points in the parameter space of model \mathcal{M} , $\vec{\theta}_i \in \Omega_{\mathcal{M}}$ (typically of the order 10^5). The details of the distribution of the points do not matter in the limit of a large number of parameter points. Each point is projected onto the corresponding euclideanized signal, $\vec{x}_i = \vec{x}(\vec{\theta}_i)$. This projection depends on the details of the detector. If multiple experiments are used, the corresponding vectors are concatenated. Euclideanized signals are generated using *swordfish* [30] (see paper for technical details). This process essentially provides a sample of the model parameter space \mathcal{M} embedded in the (usually higher dimensional) euclideanized signal space. In addition, the mapping between these spaces is known if \mathcal{M} is sufficiently sampled. This sample of parameter points and corresponding euclideanized signals are the basis for the various estimation techniques used in this work.

Confidence contours. Given the sample of projected points, \vec{x}_i , it is now straightforward to generate expected contours around any parameter $\vec{\theta}_0 \in \Omega_{\mathcal{M}}$ in the model parameter space. Such regions are for instance shown in Fig. 1. To this end, we first calculate the projected signal $\vec{x}_0 = \vec{x}(\vec{\theta}_0)$. Then, using standard nearest neighbor finder algorithms [68], we identify the set of points $\vec{\theta}_i$ that are within a radius $r_{\alpha}(\mathcal{M})$ of point $\vec{\theta}_0$. Here, $r_{\alpha}(\mathcal{M})$ depends on the dimensionality of the parameter space $\Omega_{\mathcal{M}}$ as well as the significance level of interest, $r_{\alpha}(\mathcal{M}) = \sqrt{\chi_{k=d, \text{ISF}}^2(1-\alpha)}$ where $\chi_{k=d, \text{ISF}}^2$ is the inverse survival function of the Chi-squared distribution with $k = d$ degrees of freedom. For the 3-dim models that we consider in this paper, and a significance level of $\alpha = 0.045$, we have for instance $r_{\alpha}(\mathcal{M}) = 2.84$. Now, the points in the model parameter space $\Omega_{\mathcal{M}}$ that belong to the confidence region can be simply identified by back-projecting the nearest neighbors in euclideanized signal space (obviously this back-projecting just requires a look-

up in the original list of model parameters). In this way, the generation of confidence regions around arbitrary signal points is efficiently achieved.

Number of distinct signals. For Fig. 2 we are interested in the (maximum) number of points that can populate the model parameter space $\Omega_{\mathcal{M}}$ such that the model points can be discriminated in the sense of Eq. (1). This is equivalent to finding the maximum number of points in the euclideanized signal space that can populate the embedding of $\Omega_{\mathcal{M}}$ such that their mutual distance is at least $r_{\alpha}(\mathcal{M})$. We derive an estimate for this number with the following procedure: For each projected sample point \vec{x}_i , we calculate the number of nearest neighbors N_i within a distance $r_{\alpha}(\mathcal{M})/2$. This can be rather efficiently done using standard clustering algorithms. Now, we assign a weight to point \vec{x}_i , which is simply given by $w_i = 1/N_i$. It hence corresponds to the ‘fractional contribution’ of a single parameter point to a confidence region. The number of distinguishable signals is given by the sum

$$\nu_{\mathcal{M}, X}^{\alpha}(\Omega_{\mathcal{M}}) = c_{ff} \sum_i w_i. \quad (\text{A1})$$

Here, c_{ff} is a filling factor correction related to the packing density of hyperspheres in a d -dim parameter space. For the 3-dim models in which we are often interested, this number is given by $c_{ff} = 0.74$ [69]. We find that this prescription provides an efficient and reliable way to estimate the number of distinct signals of a model. The main requirement in the calculation is that each of the potential confidence regions contains a sufficiently large (typically at least ten) number of samples. Adding more points to the original list would then not affect the result anymore. We tested the stability of our results by doubling the number of sampled points in various examples from the text. The results remained unchanged in the limit of ten points per distinct region.

Distinct signals compatible with \mathcal{H}_0 . We are interested in the fraction of the distinct signal points that are consistent with a null hypothesis that is defined as a lower dimensional subspace of the full model parameter space, $\Omega_{\mathcal{S}} \in \Omega_{\mathcal{M}}$. Here, we call a point in $\Omega_{\mathcal{M}}$ ‘consistent’ with $\Omega_{\mathcal{S}}$ if the composite null hypothesis $\Omega_{\mathcal{S}}$ cannot be excluded against the alternative hypothesis $\Omega_{\mathcal{M}}$. To estimate this number, we first generate a large number of points in $\Omega_{\mathcal{S}}$. We then collect all points from the original sample of $\Omega_{\mathcal{M}}$ whose minimum distance to any of the points from $\Omega_{\mathcal{S}}$ is smaller than the threshold values $r_{\alpha}(\mathcal{M}, \mathcal{S})$. Here, the threshold is derived from a χ_k^2 distribution with k degrees of freedom, where k is the difference in the dimensionality of $\Omega_{\mathcal{M}}$ and $\Omega_{\mathcal{S}}$ (for the examples in the paper, we usually have $k = 1$, and hence $r_{\alpha}(\mathcal{M}, \mathcal{S}) = 2$). The number of distinct signals that are compatible with the null hypothesis $\Omega_{\mathcal{S}}$ is then simply obtained by restricting the sum in Eq. (A1) to the points within the shell around $\Omega_{\mathcal{S}}$.

Parameter ranges and nuisance parameters. Finally, the contours in Fig. 3 and Fig. 4 are generated by identifying all points that are consistent with the indicated

null hypotheses, as described in the previous paragraph. However, in these figures we also take into account the effects of DM halo uncertainties, as described in the main text (this is not easily possible when calculating the number of dimensions). To this end, we generate for each point $\vec{x}_i \in \Omega_{\mathcal{M}}$ several euclideanized signals corresponding to various randomly selected DM halo configurations. Again, the specific distribution of these points does not matter as long as the number is large enough to sufficiently cover the various halo configurations. In order to incorporate external constraints on the DM halo parameters, we add an additional contribution to the euclideanized distance calculation, which is just given by $(\eta_i - \bar{\eta})^2 / \sigma_{\eta}^2$, where $\bar{\eta}$ and σ_{η}^2 are the mean and variance of the nuisance parameter, and η_i is the value of the nuisance parameter for a specific point i . The contribution to the $\vec{x}(\vec{\theta})$ is a simple concatenation of $(\eta_i - \bar{\eta}) / \sigma_{\eta}$ with the Euclideanised signal.

For a large number of sampled points this approach exactly matches a profile log-likelihood analysis. We check this limit is saturated by increasing the number of sampled points until our results do not noticeably change.

Appendix B: Dark matter signal modeling

Halo Uncertainties. We incorporate halo uncertainties [57] by assuming Gaussian likelihood distributions for three parameters of the Maxwellian velocity distribution of DM: the Sun’s speed $v_{\odot} = (242 \pm 10)$ km/s [70], the local circular speed $v_c = (220 \pm 18)$ km/s [71], and the Galactic escape speed $v_{\text{esc}} = (533 \pm 54)$ km/s [72]. We assume that these uncertainties are uncorrelated [73], though in general correlations coming from the modeling of the Milky Way halo can be included [74, 75]. We sample from these distributions as nuisance parameters in our signal calculation and include an additional penalization term to the euclideanized signal in Eq. (1).

Detector specifications. We implement a simplified XENON1T for which we adopt an S1-only analysis, full details of which are given in Sec. IIIB of [30]. For the recoil spectrum dR/dS_1 , we use 19 bins linearly spaced between 3 and 70 PE (corresponding to nuclear recoil energies $E_R \in [5, 40]$ keV). The number of bins was chosen for computational efficiency with no noticeable loss in accuracy. We have checked that including a 20% energy resolution [76] and increasing the number of bins should have no substantial effect on our results. Background distributions as a function of S_1 are described in Fig. 3 of [6] for which we assume 1% uncertainty on all components separately. We also sum over different Xenon isotopes, weighting by their naturally-occurring mass fractions [77].

For our future Xenon detector we scale up the observation time of XENON1T-2017 by a factor of 100, assuming that background rates stay constant. This exposure roughly corresponds to that expected for the full run of

the XENONnT experiment [60], so we will refer to this future detector as *XENONnT*.

DarkSide20k: We directly use the recoil energy spectrum dR/dE_R as our signal, assuming that the only relevant isotope is Argon-40. We follow the specifications of the Darkside50 detector [78], with the nuclear recoil efficiency taken from Fig. 6 in [78]. The background is assumed to be flat across the entire energy range with an expected 0.1 events (with 10% uncertainty) over 1422 kg days of observation. We assume 19 linearly spaced bins between 32 and 200 keV.

For our future detector, we assume an exposure of 7.3×10^6 kg days, corresponding to a 1-year exposure with a 20-tonne detector. We assume that the background will remain at 0.1 events in the total exposure. This detector configuration roughly resembles *DarkSide20k* [62].